Journal of Basics and Applied Sciences Research (JOBASR)
ISSN (print): 3026-9091, ISSN (online): 1597-9962
Volume 3(4) July 2025
DOI: https://dx.doi.org/10.4314/jobasr.v3i4.24

Zinc Oxide Nanoparticles Produced from Pumpkin Pods and Zinc Acetate as Corrosion Inhibitor on Aluminium Metal in Acidic Medium: Kinetics and Thermodynamics Study

Akakabota, A.O.[1] & Okewale, A. O.[2]
[1&2]Department of Chemical Engineering, Federal University of Petroleum Resources, Effurun, P. M. B., 1221, Delta State
[*]Corresponding Author Email: akakabota.ambrose@fupre.edu.ng, ORCID ID:0009000486441727

ABSTRACT
This study investigates the kinetic and thermodynamic potential of using zinc oxide nanoparticles produced from pumpkin pods and zinc acetate as corrosion inhibitors on Aluminium metal immersed in an acidic medium. Kinetics and thermodynamic studies of the corrosion process are crucial for analysing and controlling corrosion processes. The corrosion study was conducted using an electrochemical spectroscopy method at temperatures of 35°C, 45°C, and 55°C. The kinetic study was analysed using Open Circuit Potential (OCP) and Linear Polarisation Resistance (LPR) for a 1.0MHCl Solution. The electrochemical measurement shows that the inhibitor concentration exhibits better corrosion resistance than the control, indicating that the coated sample provides an inhibitive effect against the entrance of the hydrochloric acid solution into the active site of the metal. This zinc oxide nanoparticle acts predominantly as an anodic, cathodic, and mixed-type inhibitor. The results show that using varying inhibitor dosages of 30 ppm, 110 ppm, and 190 ppm reduces the corrosion of aluminium metal in a hydrochloric acid environment. The polarisation resistance and corrosion rate results from the LPR and OCP measurements confirmed the effectiveness of this inhibitor. The corrosion rate from the electrochemical test indicated a gradual decrease as the dosage of the inhibitor increased, resulting in increased polarisation resistance. The results show a higher activation energy for the inhibited process at 110 ppm in comparison with the control, indicating that the inhibitor hinders the corrosion of aluminium metals. Conversely, this is not the case for 30 ppm and 190 ppm. This trend suggests that the inhibited process at a 110 ppm dosage is due to physisorption, while chemisorption occurs at 30 ppm and 190 ppm, respectively. The enthalpy change (ΔH) for 30 ppm, 110 ppm, and 190 ppm solutions are 242,881.4 J/mol, 147,632 J/mol, and 95,266.6 J/mol, respectively, which is higher than that of the control (65,487.1 J/mol). Both enthalpy change and entropy change (ΔS) values are positive, indicating that the adsorption on the aluminium metal is endothermic and increases the rate of disorderliness of the process.

Keywords:
Pumpkin Pod,
Energy Dispersive X-ray Spectroscopy
Scanning Electron Microscopy,
Brunauer-Emmett-Teller Surface Area Analysis,
Open Circuit Potential,
Linear Polarization Resistance.

INTRODUCTION

Corrosion is an occurrence that can be chemical or physical in origin (Zehra*et al*., 2022), denatures the mineral features of alloys, and renders them ineffective for a certain function (Quadri *et al*., 2022). Alloy corrosion is mostly caused by their propensity to return to a stable form (Esquivel & Gupta, 2020). Most alloys are naturally unstable (Liu *et al*., 2016) and tend to undergo self-destruction by interacting with the environment, creating metal compounds to achieve lower energy states (Garg*et al*., 2015). These were the states where most minerals were found (Dahmani *et al*., 2010). Given that numerous methods are used for determining the corrosion of alloys, using inhibitors is most appropriate method for protective covering of Alloys from solutions that are corrosive (Dahmani*et al*.,2010).

Corrosion inhibitors are chemicals added in small amounts to corrosive environments to help protect metals from reacting with those environments (Popov, 2015). Many of the organic inhibitors commonly used today are quite costly (Ahmad et al., 2010).

How to cite this article: Akakabota, A.O. & Okewale, A. O. (2025). Zinc Oxide Nanoparticles Produced from Pumpkin Pods and Zinc Acetate as Corrosion Inhibitor on Aluminium Metal in Acidic Medium: Kinetic and Thermodynamic Study. *Journal of Basics and Applied Sciences Research*, 3(4), 203-215. https://dx.doi.org/10.4314/jobasr.v3i4.24

The effectiveness of an inhibitor on mild steel depends on several factors, including the steel's properties, the type of solution it is in, and the structure of the inhibitor molecule (Junaedi *et al.*, 2013). When used on aluminium, these inhibitor molecules attach themselves to the metal's surface, forming a protective layer that blocks both anodic and cathodic reactions. Some of these inhibitors can also chemically interact with iron atoms on the aluminium surface, creating stable inorganic compounds that further shield the metal (Junaedi et al., 2012). Given the high cost, toxicity, and environmental concerns of synthetic inhibitors, researchers are increasingly exploring plant-based alternatives as a safer and more sustainable option (Oguzie *et al*., 2007).

Nanotechnology involves the study and application of science, engineering, and technology at the nanoscale, typically between 1 and 100 nm (Hulla *et al*., 2015). Green synthesis of nanoparticles uses natural, eco-friendly, and affordable materials, like plant extracts, microbes, and other biological sources, as reducing and stabilizing agents. By avoiding toxic chemicals, this approach helps minimize health and environmental hazards right from the start (Iravani, 2011). Studying kinetics and thermodynamics is crucial in understanding the process of corrosion mitigation (Ituen *et al*., 2017). These studies offer insights into the interaction mechanisms between inhibitors and metal surfaces, which are essential for developing effective corrosion prevention strategies (Liu *et al*., 2024). Thermodynamic parameters further elucidate the spontaneity and nature of the adsorption process, which is vital for predicting the efficiency of corrosion inhibitors under various conditions (Aslam *et al*., 2022).

In this study, a nanoparticle produced from pumpkin pod extract and zinc acetate was employed as a green corrosion inhibitor on aluminium in an acidic medium, due to its economic value and eco-friendly nature.

MATERIALS AND METHODS

The materials utilised in this study include the following: pumpkin pods, aluminium metals, concentrated hydrochloric acid (HCl), zinc acetate ($ZnC_4H_6O_4$), distilled water, detergents, acetone, and ethanol. All the reagents are of analytical grade from Sigma Aldrich.

Instrument and Apparatus

The apparatus used in this study are; hacksaw (48 – 22 – 0050), weighing balance (MAB220), oven (H – 30105), water bath (TSCIR19), magnetic stirrer (MS500), soxhlet extractor (LC – 122), conical flask (1122 – 150), beakers (GW – 30), measuring cylinder (740644), and electrochemical spectroscopy (PGSTAT101).

Synthesis of Zinc Oxide Nanoparticles (ZnONP)

The pumpkin pods were purchased from a local market in Agbarho, Delta State, Nigeria. The extraction and synthesis procedure followed the methods employed by Haque et al. (2020) and Elemike et al. (2021), with slight modifications. In this synthesis procedure, 50 mL of the aqueous extract from pumpkin pods (*Telfairiaoccidentalis*) and 500 mL of 0.01 M zinc acetate solution were mixed at a ratio of 1:5, with the addition of 25 mL of NaOH solution added in dropwise. The resulting mixture was stirred continuously on a magnetic stirrer at 75 °C for 4 hours. During this reaction time, the colour of the colloidal solution gradually changed from light brown to a cream-coloured solution, indicating an increase in the rate of bio-reduction of the zinc acetate and the formation of a zinc hydroxide ($Zn(OH)_2$) precipitate.

Characterisation of Zinc Oxide Nanoparticles

The zinc oxide nanoparticle synthesised from pumpkin pod extract was characterised using the following: Ultraviolet-visible spectroscopic, Fourier transform infrared spectroscopy (FTIR), energy dispersive x-rays (EDX), scanning electron microscopy (SEM), Brunauer-Emmett-Teller analysis (BET) and X–ray diffractogram (XRD).

Ultraviolet-Visible Spectroscopy

A colour change initially confirmed the formation of zinc oxide nanoparticles. After the colour change, further confirmation of the synthesised zinc oxide nanoparticles was obtained by scanning the absorption spectra within the range of 300-800 nm using a double-beam Ultraviolet-Visible Spectrophotometer (Kalpana *et al*., 2018).

X-Ray Diffraction

X-ray diffraction (XRD) is a non-destructive method commonly used to analyze and identify corrosion-related materials (Dang *et al*., 2022). It offers detailed insights into a material's structure, including its phases, orientation, grain size, crystal defects, and overall crystalline composition, helping with accurate material identification. (Pandey *et al*., 2021). Analysis of the X-rays provides an elemental analysis of the surface composition without altering the nature of the object under examination. The samples (zinc oxide nanoparticles) were run on the X-ray Diffractometer. Running test material from 10° 2-theta to 90° 2-theta with a 0.02 step size and a 2-second step time were the conditions of analysis. The International Centre for Diffraction Data (ICDD/JCPDS) database standards were used to compare each crystalline phase (López & Rodriguez, 2017).

Scanning Electron Microscopy (SEM)

The size and shape of the synthesised zinc oxide nanoparticles were examined at various magnifications using a scanning electron microscope operating at 10kV. Scanning electron microscopy is a technique used for the observation and characterisation of materials on a nanometre to micrometre scale. The SEM provides high-resolution and long-depth-of-field images of the sample surface and its near-surface region. The basic principles involved in SEM consist of bombarding the surface sample to be examined under vacuum with a finely focused beam of electrons. A very fine, focused beam of electrons is scanned over the specimen's surface (Al-Dhabi & Valan, 2018).

Fourier Transform Infrared Spectroscopy (FTIR)

The structural organisation of the synthesised zinc oxide nanoparticle was investigated to identify the functional group present. The nanoparticles were examined using a Buck Scientific infrared spectrophotometer with the range 4000 – 500 cm-1 (wavenumber) with a resolution of 2 cm-1. These FTIR spectroscopy studies establish the biomolecules responsible for the stabilisation and capping of zinc oxide nanoparticles (ZnONP). The sample was freeze-dried and obtained in a powdered form (Kumar *et al*., 2015).

Energy Dispersive X-Ray Spectroscopy (EDX)

The Energy-dispersive X-ray spectroscopy is carried out by using a high-energy beam of charged particles, such as electrons or photons or a beam of X-rays, being focused onto the sample. The incident beam excited an electron inside the shell, ejecting it from the shell and creating an electron hole. An electron from an outer shell can fill this hole with the emission of an X-ray. A measurement of the energy of the X-rays emitted from the specimen is then used to determine its elemental composition (Martin *et al*., 2002).

Brunauer-Emmett-Teller (BET)

The Brunauer-Emmett-Teller method is the most commonly used method to determine the surface area and pore volume of nanoparticles (Morones *et al*., 2005). This method was carried out to directly measure the specific surface area and pore sizes of powdered samples under high-vacuum conditions. In a typical BET analysis, the surface area of the nanoparticles is determined from the volume of N_2 gas adsorbed on the powdered sample at a temperature of 77K. N_2 gas is assumed to have access to the entire nanoparticle surface (Ochiai&Fujishima, 2012).

Electrochemical Spectroscopy

According to the ASTM G3/G102 standard procedure for electrochemical measurements, the electrochemical test was conducted using a 1 M HCl solution in a glass cell containing 100 mL of the solution as the test medium. A potentiostatgalvanostat (PGSTAT 101) was employed, and aluminium metal was used as the working electrode (WE) in the common three-neck electrode arrangement. A graphite rod serves as the counter electrode, and a glass body calomel electrode (of the Onesil brand) with a silver/silver chloride 3 M KCl solution as the reference electrode.

The 25-mm-long graphite rod was immersed in the test solution. The working electrode (W_E) was welded to a copper wire and mounted on an epoxy resin, leaving an exposed surface area of 1515 mm² to the solution. The experiment was conducted inside a glass cell containing 100 mL of electrolyte at three distinct temperatures: 35°C, 45°C, and 55 °C. The NOVA2.1.2 software linear sweep voltammogram staircase was calibrated using an open-circuit potential (OCP) with a start potential of -1.5 V and a stop potential of 1.5 V at a scan rate of 0.005 V/s. The test was conducted over 60 minutes.

To ensure reproducibility, the experiment was repeated three times on a specimen with the same composition, and the OCP of each test sample was noted. Corrosion potential (E_{corr}), corrosion density (J_{corr}), anodic slope (αa), and cathodic slope (αc) were obtained using Tafel plot extrapolation. The corrosion rate (C_R) and polarisation resistance (PR) were calculated from these derived parameters using Equations 1 and 2, respectively.

$$C_R = \frac{(0.00327 \times 5 \times j_{corr} \times w_{eq})}{p} \qquad (1)$$

Where J_{corr} is the corrosion current density per square cm, ρ is the density of the material in g/cm^3, and w_{eq} is the equivalent weight of the material in grams. The corrosion rate values were expressed in millimetres per year (mm/yr).

$$P_R = \frac{(2.303 \times b_a \times b_c)}{j_{corr}(b_a + b_c)} \qquad (2)$$

nmKinetic Study

The linear polarisation resistance (LPR) and open-circuit polarisation were used to investigate kinetic parameters, including corrosion rate and current density. The Arrhenius equation was used to calculate the activation energy at different temperatures (35°C, 45°C, and 55°C), using Equation 3 (Goni et al., 2024).

$$C_R = \log K - \frac{Ea}{2.303RT} \qquad (3)$$

C_R is the corrosion rate (mm/yr), T is the temperature (^{o}C), R is the universal gas constant, and E_a is the activation energy (Goni *et al*., 2024).

Thermodynamics Study

Thermodynamic parameters, such as enthalpy (ΔH) and entropy (ΔS), were investigated using the Arrhenius transition state equation, as given in equation 4 (Ezeibe *et al*., 2019).

A plot of log (C_R/T) against (1/T) gives a slope of (-ΔH/2.303R) and intercept $\left\{\log \frac{R}{Nh} + \frac{\Delta S}{2.303R}\right\}$.

$$\log \frac{C_R}{T} = -\frac{\Delta H}{2.303RT} + \left\{\log \frac{R}{Nh} + \frac{\Delta S}{2.303R}\right\} \qquad (4)$$

RESULTS AND DISCUSSION

Characterisation of Zinc Oxide Nanoparticles

UV-Visible Spectroscopy

UV-Vis spectroscopy is usually the first instrumental technique used to monitor the progress of nanoparticle synthesis. This is because it reveals relevant information on the formation of particles in the nano range (Jimoh *et al*., 2022). Figure 1 shows the UV-vis spectral result of the biosynthesized ZnONP. The absorbance of the nanoparticles was observed at 341 nm. This provides insight into the reduction activity and formation of ZnONP, which can be attributed to the intrinsic bandgap of ZnO, spanning from the valence to the conduction bands, resulting from electronic transitions (Kovo*et* al., 2021). This gives excellent agreement with those previously reported in the literature by Hairui*et al*. *(*2020). The immediate white-yellowish colour appearance at the start of the reaction synthesis indicates that the reaction proceeds towards the formation of ZnONPs. This is attributed to Surface Plasmon Resonance (SPR), resulting from the combined oscillation of free electrons (Prami *et al*., 2019).

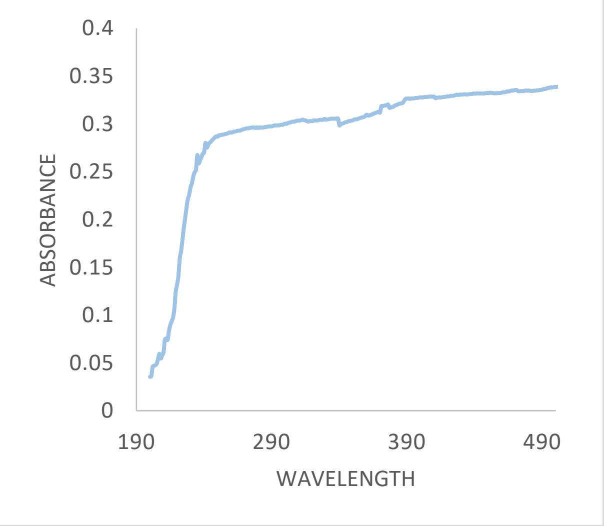

Figure 1: UV-Visible Spectral for ZnONP

Fourier Transform Infrared (FTIR)

The FTIR spectra shown in Figure 2 provide information about the reactive functional groups present in the biosynthesised ZnONPs. The peaks, which range from 4000 cm^{-1}to 500 cm^{-1}, as indicated by the spectral data, help differentiate the biomolecules involved in reducing the metals in the precursor into ZnONPs in conjunction with the plant extract. The peak at 760 represents the carbon-hydrogen bend bonding on the ZnONPs, and a similar observation was also reported by Hamid *et al*. (2022). The peak at 3384 cm^{-1} corresponds to the O–H stretch vibrations of phytochemicals, which may be present on the surface of the nanoparticles (Nzeke et *al*., 2019). The Zn–O stretching vibrations and ZnO bond were indicated by the peaks at 898 cm^{-1} and 682 cm$^{-1,}$ respectively, which affirm the successful completion of the synthesis of the ZnONPs (Kovo et *al*., 2021). The peak at 1558 cm^{-1} may be attributed to the stretching vibration of zinc carboxylate (COO-Zn). These reactive groups (Zn-OH and COO-Zn) at the surface of the nanoparticles can play an important role as reaction active sites (Donya *et al*., 2013).

Table 1: FTIR information of ZnONP

Peak Number	Wavenumber (cm^{-1})	Reactive Groups
1	682.10282	Zn-O bond
2	760.37692	C-H bend
3	898.28842	Zn–O stretch
4	1401.4790	C-H scissoring,
5	1509.5718	C=O
6	1558.0272	(COO-Zn)
7	3384.4227	O-H Stretch

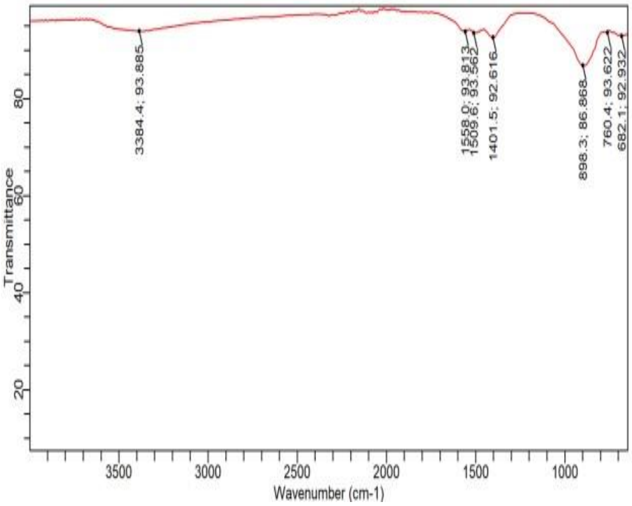

Figure 2: FTIR information of ZnONP

Scanning Electron Microscopy (SEM)

Figure 3 shows the SEM micrograph of the synthesised ZnONP. The essence of Scanning Electron Microscopy is to unveil the structure of the surface and the actual morphology of the nanoparticles. ZnONP are shown to have an irregular shape, porosity, and surface structure in the micrograph, which enables the ZnONP to serve as an inhibitor in the corrosion investigation, consistent with the porous measurement in BET. The porous surface visible in the micrograph provides a hint as to how the nanoparticles may be used in the investigation of corrosion, catalysis, and the adsorption of molecules. Similar observations have been discussed in previous research by Kovo et al. (2021) and Jimoh et al. (2022) about its morphology and importance in application.

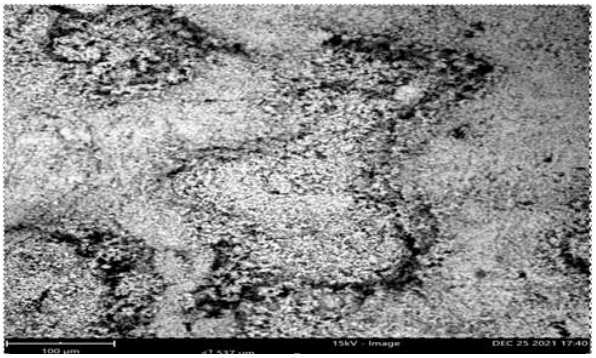

Figure 3: SEM Micrograph of ZnONP

Energy Dispersive X-Ray Analysis (EDX)

Figure 4 is the Energy Dispersive X-ray analysis (EDX) spectrum for the synthesised ZnONP. The spectrum clearly showed all the elemental components present in the synthesised ZnO nanoparticles. It revealed the presence of sodium, zinc and oxygen in their percentage composition and weight concentration. According to the elemental analysis in Table 2, Zinc has the highest percentage composition and weight concentration, at 50.75%, and oxygen at 7.96%, indicating the successful synthesis of ZnONP. A similar observation was described in past literature (Kovo*et al*., 2021; Ismail *et al.*, 2018). Meanwhile, alkali earth metal elements, such as sodium, were also observed in the signal at a normal mode, which may be attributed to part of the constituents used in synthesising the precursor applied in the synthesis of the ZnO nanoparticles.

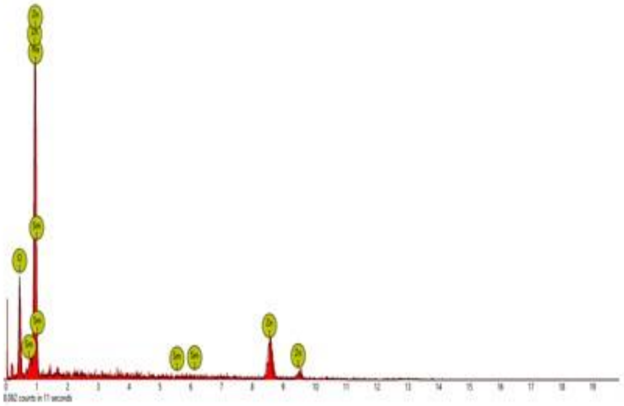

Figure 4: EDX Spectral of ZnONP

Table 2: Elemental analysis

Element Number	Element Symbol	Element Name	Weight Conc.
11	Na	Sodium	41.29
30	Zn	Zinc	50.75
8	O	Oxygen	7.96

Brunauer-Emmett-Teller (BET)

Table 3 describes the BET analysis of the ZnONP, which revealed the surface area of the nanoparticles as 6.464 m²/g. A similar result was obtained by Alharbi *et al*. (2021), Gharpure et al. (2022), and Mureddu *et al*. (2014), who demonstrated that the surface area of ZnONPis 6.032 m²/g. From the literature, materials have been classified into three categories: microporous, mesoporous, and macroporous, depending on the size of pore diameters. Materials having a pore diameter less than 2 nm are called microporous, materials ranging between 2 and 50 nm are called mesoporous, and those with a pore diameter greater than 50 nm are called macroporous or non-porous (Kamegawa *et al.*, 2019). The BET result showed that the synthesised ZnONP is mesoporous and has significant applications in the adsorption of molecules at extremely low pressures (Ismail *et al.*, 2018). The report by Yu et al. (2010) explained that mesoporous materials offer advantages for photocatalytic reactions and corrosion inhibition. Therefore, quantities of specific surface area, which are determined through the BET method, may depend on the adsorbate molecule used and its adsorption cross-section in the adsorption experiment (Hana et *al.*, 2014).

Table 3: Surface feature of the ZnONP

Material	**Surface area (m^2/g)**
ZnO Nanoparticles	6.464

However, Figure 5 further indicated that the 30 ppm ZnONP and 110 ppm ZnONP coatings acted predominantly as cathodic corrosion protective coatings. In comparison, the 190 ppm ZnONP coating acted predominantly as an anodic corrosion protective coating (Hamindon&Hussin, 2020). Moreover, Figure 6 displays the OCP versus time curves of the sample, which indicates that the sample exhibited stable state potentials between 50 and 120 seconds of immersion. (Benoit et al., 2021).

Table 4: Tafel data for aluminium and ZnONP inhibitors 1.0 M HCL 35 ºC

Inhibitor Dosage (ppm)	**Ecorr, Obs (V)**	**Jcorr (A/cm2)**	**C_R (mm/year)**	**P_R (ohms)**	**Ecorr, Calc (V)**	**[ba] (V/dec)**	**[bc] (V/dec)**
Control	-1.0737	7.1647×10^{-7}	0.083253	4.5389×10^{5}	-1.5552	2.0211	1.18950
30	-1.2355	2.0277×10^{-7}	0.0023562	5.6899×10^{5}	-1.0506	0.95531	0.367980
110	-1.1462	1.6751×10^{-7}	0.0019465	8.4726×10^{5}	-1.1137	0.91846	0.507280
190	-0.83049	2.7132×10^{-7}	0.000315270	3561	-0.83353	0.036958	0.055893

Kinetic Study

Table 4 and Figure 5 display the polarisation data and polarisation curves for aluminium and the ZnONP inhibitor in 1 M HCl at 35°C, respectively. The 30 ppm ZnONP exhibited better corrosion resistance than the control sample. In contrast, the control sample had a corrosion rate (C_R) of 0.083253 mm/year, corrosion current density j_{corr} of 7.1647×10^{-7}Acm^{-2} and polarization resistance (P_R) of 4.5389 $\times 10^{5}\ \Omega$. The 30 ppm dosage of ZnONP coated sample exhibited a lower C_R of 0.0023562mm/ year, low j_{corr} of 2.0277×10^{-7}Acm^{-2} and high P_R of $5.6899\times 10^{5}\Omega$, this indicates that the 30 ppm ZnONP coated sample provided better inhibitive effect against the entrance of the Cl^- ions into the active sites of the aluminum metal (Fayomi&Akande, 2019).

The 30 ppm ZnONP coating was observed to exhibit better corrosion resistance compared to the 190 ppm ZnONP coating. Relative to the entire sample, the 110 ppm ZnONP-coated sample exhibited the lowest C_R of 0.0019465mm/year and the lowest j_{corr} of 1.6751×10^{-7}Acm^{-2}, and higher polarization resistance $8.4726\times 10^{5}\Omega$. This indicated that the 190 ppm ZnONP provided the least corrosion resistance, with an impedance of 3561 Ω, against the deteriorating effect of the corrosive ions from the 1.0 M HCl solution at 35 °C. The reason for this could be the doping effect of the ZnO nanoparticles, which provides a supportive covering against the diffusion of chloride to the anodic and cathodic sites of the aluminium metal (Pan *et al*., 2018).

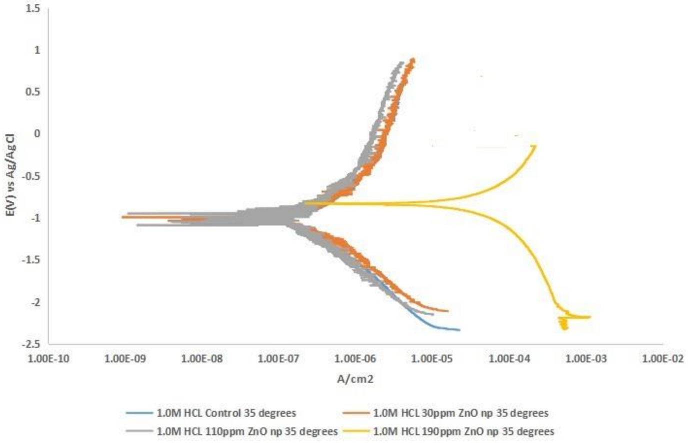

Figure 5: LSV Plot for Aluminium and ZnONP Inhibitor 1.0 M HCl at 35 ºC

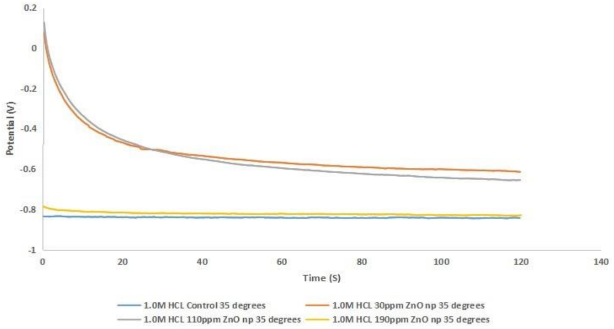

Figure 6: OCP Plot for Aluminium and ZnONP Inhibitor 1.0 M HCl at 35 ºC

Table 5 and Figure 7 display the polarisation data and polarisation curves for the corrosion inhibition of aluminium metal using a ZnONP inhibitor in 1.0 M HCl at 45°C, respectively. The 30 ppm ZnONP exhibited better corrosion resistance than the control sample, as shown in Table 2. This indicates that the 30 ppm ZnONP-coated sample provided a better inhibitive effect against the adsorption of the HCl solution onto the active sites of the aluminium metal (Fayomi& Akande, 2018). The 30 ppm ZnONP coatings exhibited better corrosion resistance compared to both the 110 ppm and 190 ppm ZnONP coatings. Relative to the entire sample, the 30 ppm ZnONP-coated sample exhibited the lowest CR 0.00195530 mm/year and the lowest j_{corr} of 1.6827× 10^{-6}Acm^{-2}, and higher polarization resistance 1.1016E06Ω, respectively. This indicated that the 190 ppm ZnONP coating provided the least corrosion resistance (151.0600 Ω) against the deteriorating effect of the corrosive ions from the 1.0 M HCl solution at 45 °C. The reason for this could be the doping effect of the ZnO nanoparticles, which provides a supportive covering against the diffusion of chloride to the anodic and cathodic sites of the aluminium metal (Pan et al., 2018).

However, Figure 7 further indicated that the 30 ppm ZnONP and 190 ppm ZnONP coatings acted predominantly as cathodic corrosion protective coatings while 110 ppm ZnONP acted predominantly as an anodic corrosion protective coating (Hamindon&Hussin, 2020). Moreover, Figure 8 displays the OCP versus time curves of the samples, indicating that the samples exhibited a stable state potential between 90 and 120 seconds of immersion time (Fayomi et al., 2019).

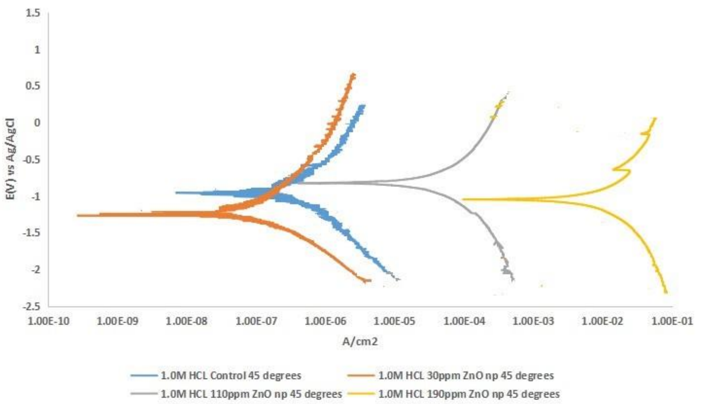

Figure7: LSV Plot for Aluminium and ZnONP inhibitor for 1.0 M HCl at 45ºC

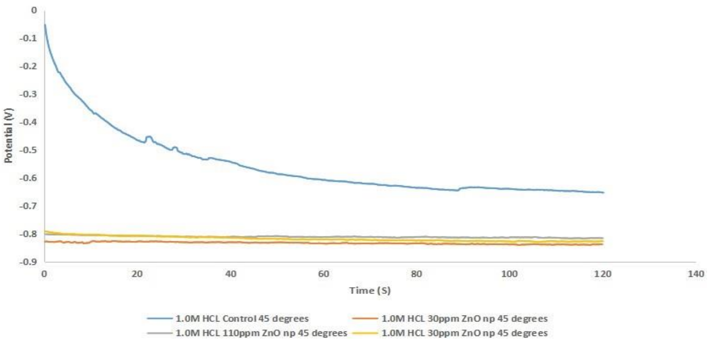

Figure 8: OCP Plot for Aluminium and ZnO NP Inhibitor 1.0 M HCl at 45 ºC

Table 5: Tafel data for aluminium and ZnONP inhibitor 1.0 M HCl 45 ºC

Inhibitor Dosage (ppm)	Ecorr, Obs (V)	Jcorr (A/cm^2)	C$_R$ (mm/year)	P$_R$ (ohms)	Ecorr,Calc (V)	[ba] (V/dec)	[bc] (V/dec)
Control	-0.97865	8.7482$\times 10^{-7}$	0.0101650	3.787$\times 10^{5}$	-0.90952	2.2234	1.16120
30	-1.2653	1.6827$\times 10^{-7}$	0.0195530	1.1016$\times 10^{6}$	-1.13990	-1.56310	1.14410
110	-0.82203	4.2509$\times 10^{-7}$	0.0493950	3817.000	-0.81711	0.098335	0.060274
190	-1.04530	1.5583$\times 10^{-7}$	0.1810700	151.0600	-1.03590	0.010205	0.011559

Table 6 and Figure 9 display the polarisation data and polarisation curves for aluminium and ZnONP inhibitor at 1.0 M HCl at 55°C, respectively. The 30 ppm ZnONP exhibited the least corrosion resistance of the control sample. In contrast, the control sample possessed the corrosion rate (C_R) of 0.0042575 mm/year, corrosion current density, jcorr of 3.6640×10^{-7}Acm^{-2} and polarization resistance (P_R) of $7.1064\times 10^{5}\,\Omega$, the 30 ppm ZnONP coated sample exhibited C_R of 0.8108900 mm/ year, j_{corr} of 6.9784×10^{-8}Acm^{-2} and a low P_R of 63. 098 Ω. This indicates that the 30 ppm ZnONP-coated sample provided the least inhibitive effect against the entrance of the HCl solution onto the active sites of the aluminium metal (Fayomi& Akande, 2018). The 30 ppm ZnONP coating exhibited the least corrosion resistance compared to the 110 ppm ZnONP and 190 ppm ZnONP coatings. Relative to the entire sample, the 190 ppm ZnO NP coated sample exhibited the lowest C_R of 0.0012276 mm/year and the lowest j_{corr} of 1.0565×10^{-8}Acm^{-2}, and higher polarization resistance $1.1676\times 10^{6}\Omega$. This indicated that the 190 ppm ZnONP coating provided the best corrosion resistance of $1.1676\times 10^{6}\Omega$, against the deteriorating effect of the corrosive ions from the 1.0 M HCl solution at 55 ºC. The reason for this could be the doping effect of the ZnO nanoparticles. The 190ppm ZnONPprovides more supportive coverage against the diffusion of the chloride to the anodic and cathodic sites of the aluminum metal due to more molecules on the surface of the Aluminum Metal in comparison to the 30ppm and 110ppm ZnONP (Pan *et al*., 2018). The result also shows that the corrosion rate increases as the temperature increases from 35 °C to 55 °C for all the concentrations of ZnONP investigated in this study. Notably, for 30 ppm ZnONP, the corrosion rate increases from 0.002 mm/yr to 0.81 mm/yr as the temperature increases from 35 °C to 55 °C. While for 110ppm, the corrosion rate increases from 0.0019mm/yr to 0.067mm/yr asthe temperature increases from 35 °C to 55 °C, and lastly, for the 190ppm ZnONP, the corrosion rate increases from 0.0003mm/yr to 0.0012mm/yr as the temperature increases from 35 °C to 55°C,respectively. The reason for this increase could be as a result of a decrease in activation as the temperature increases, due to a higher fraction of the molecules surpassing the activation energy, thus, accelerating the corrosion rate (Gayakwad, Patil, & Rao, 2022; Zhao *et al.*, 2022). In addition, higher temperature fosters rapid formation and growth of corrosion particles while enabling quicker ion migration, increasing localized corrosion rates (Quan, *et al*., 2021).

However, Figure 9 further indicated that the 30 ppm ZnONP and 110 ppm ZnONP coatings acted predominantly as anodic corrosion protective coatings. In comparison, the 190 ppm ZnONP coating acted predominantly as a cathodic corrosion protective coating (Hamindon&Hussin, 2020). Moreover, Figure 10 displays the OCP versus time curves of the samples, which indicates that the samples exhibited stable state potentials between 80 and 120 seconds of immersion (Fayomi et al., 2019).

Table 6: Tafel data for aluminium and ZnONP inhibitor 1.0 M HCl 55 ºC

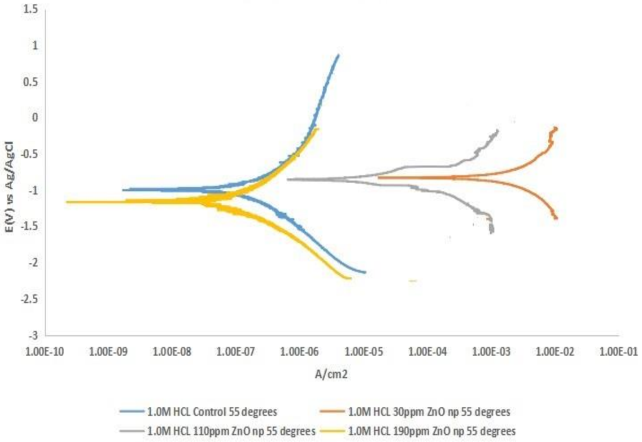

Figure 9: LSV Plot for Aluminium and ZnONP Inhibitors 1.0 M HCl at 55ºC

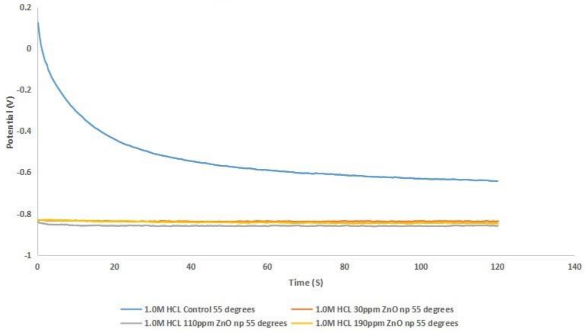

Figure 10: OCP Plot for Aluminium and ZnONP Inhibitor 1.0 M HCl at 55 ºC

Thermodynamics Parameter Study

The corrosion rate was determined at various concentrations of the inhibitor and acid solution using linear polarisation resistance measurements. The values were fitted into the Arrhenius equation to determine the best fit by comparing their R² values. The slopes obtained from the plots are therefore used in estimating the activation energy of the process at different temperatures.

Inhibitor Dosage (ppm)	Ecorr, Obs (V)	Jcorr (A/cm^2)	C_R (mm/year)	P_R (ohms)	Ecorr, Calc (V)	[ba] (V/dec)	[bc] (V/dec)
Control	-1.00450	3.6640×10^{-7}	0.0042575	7.1064×10^{5}	-0.98225	1.300900	1.112100
30	-0.83173	6.9784×10^{-8}	0.8108900	63.098	-0.82857	0.019102	0.021608
110	-0.85825	5.7480×10^{-8}	0.0667910	4590.20	-0.85511	0.162880	0.096892
190	-1.21360	1.0565×10^{-8}	0.0012276	1.1676×10^{6}	-1.23500	0.73655	0.462340

The activation energy (Ea), R², and exponential factor (K) at different inhibitor concentrations are presented in Table 7.

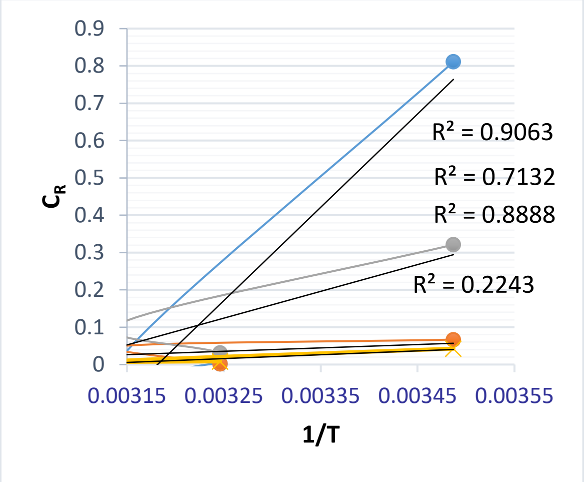

Figure 11: Plot of C_R against 1/T at 1.0M HCl

Table 7: Result of activation energy (Ea), rate constant (K), and R^2 at 1.0M HCl

Inhibitor dosage (ppm)	Ea(J/mol)	R^2	K
Control	-1976.9	0.888	0.479
30ppm	-47879.3	0.9063	0.00011
110ppm	-1730.5	0.2243	0.552
190ppm	-13738.07	0.7132	0.0062

Table 7 shows that the activation energy is higher for the inhibited process (110 ppm) than for the control, indicating that the inhibitor hinders the corrosion of aluminium metals. It is also lower for the inhibited process (30 ppm and 190 ppm) than for the control, which indicates that the inhibitor did not hinder the corrosion of the aluminium metal. This trend suggests that the inhibited process (110 ppm) is attributed to physisorption, whereas chemisorption occurs at 30 ppm and 190 ppm, respectively (Hegazy *et al.*, 2014). The corrosion rate obtained at different concentrations of the Inhibitor and acid solution from the linear polarisation resistance measurement was fitted into the Arrhenius transition equation to determine the best fit by comparing the coefficient of variation (R²) value. The slopes obtained from the plots are therefore used to estimate the enthalpy and entropy of the process at different temperatures. The enthalpy (ΔH), entropy (ΔS), and R² value at different inhibitor concentrations are presented in Table 8.

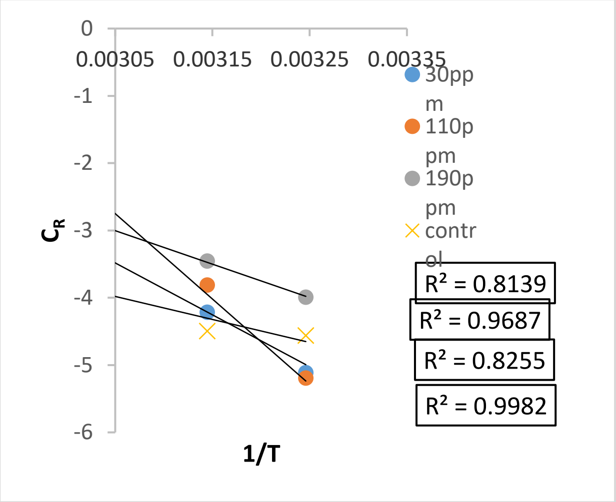

Figure 12: plot of log C_R against 1/T at 1.0M HCl

Table 8: Result of enthalpy (ΔH), Entropy (ΔS) and R^2 at 1.0M HCl

Inhibitor dosage (ppm)	ΔH(J/mol)	ΔS(J/mol)	R^2
Control	65487.05	74.07	0.8139
30ppm	242881.4	490.53	0.9687
110ppm	147632	185.9	0.8255
190ppm	95266.6	35.46	0.9982

Table 8 shows that the enthalpy change (ΔH) of the inhibited sample is higher than that of the control. The positive enthalpy change value indicates that adsorption on the aluminium metal is endothermic (Mohammed *et al.*, 2024), consistent with chemisorption (Eddy et al., 2013). The entropy change (ΔS) was positive, indicating that the disorderliness of the inhibitor on the aluminium surface increased.

CONCLUSION

The electrochemical measurement shows that the inhibitor concentration exhibited better corrosion resistance than the control. This indicates that the coated sample provided an inhibitive effect against the entrance of the hydrochloric acid solution into the active site of the aluminium metal. This coating acts predominantly as an anodic, cathodic, and mixed-type inhibitor in 1 M HCl solution. The effectiveness of this inhibitor was confirmed by the polarisation resistance and corrosion rate results obtained from the LPR and OCP measurements. The corrosion rate from the electrochemical test indicates a gradual decrease as the inhibitor concentration increases—this increased polarisation resistance. From the thermodynamic study, the enthalpy change (ΔH) obtained is higher than that of the control, and its value is positive, indicating that the adsorption of the inhibitor on the aluminium metal is endothermic and involves chemisorption. The entropy change (ΔS) was positive, indicating an increase in the rate of disorderliness of the inhibitor on the aluminium surface. The ZnONP particle behaves as a type inhibitor on the aluminium metal surface.

REFERENCE

Ahamad I, Prasad R & Quraishi M.A. (2010). Thermodynamic, Electrochemical and Quantum Chemical Investigation of Some Schiff Bases as Corrosion Inhibitors for Mild Steel in Hydrochloric acid Solutions. *Journal of Corrosion Science*, *52*, 933–942.

Akinbulumo, O. A., Oludare, J. O., & Ebenezer L. O. (2020). Thermodynamics and Adsorption Study of the Corrosion Inhibition of Mild Steel by Euphorbia Heterophylla L. Extract in 1.5 M HCl.” *Results in Materials* 5: 100074. doi:10.1016/j.rinma.2020.100074.

Alharbi, F. N., Abaker, Z. M., & Makawi, S. Z. A. (2023). Phytochemical Substances-Mediated Synthesis of Zinc Oxide Nanoparticles (ZnO NPS). *Inorganics*, *11*(8), 328. https://doi.org/10.3390/inorganics11080328

AL-Dhabi, N. A., & Valan Arasu, M. (2018). An environmentally friendly green approach for the production of zinc oxide nanoparticles and their antifungal, ovicidal, and larvicidal properties. *Nanomaterials*, *8*(7), 500.

Annon, I. A., Ahmed S. A., W. K. A., Mahdi M. H., A. A. A., Wan N. R. W. I., & Abdul Amir, H. K. (2022). Corrosion Inhibition of Mild Steel in Hydrochloric Acid Environment Using Thiadiazole Derivative: Weight Loss, Thermodynamics, Adsorption and Computational Investigations. *South African Journal of Chemical Engineering* 41: 244–52. doi:10.1016/j.sajce.2022.06.011.

Aslam, R., Mobin, M., Zehra, S., & Aslam, J. (2022). A comprehensive review of corrosion Inhibitors are employed to mitigate stainless steel corrosion in different environments. *Journalof Molecular Liquids*, *364*, 119992.

Benoit, M. J., Ogunsanya, I. G., Winkler, S., Worswick, M. J., Wells, M. A., & Hansson, C. M. (2021). Internal corrosion of warm-formed aluminium alloy automotive heat exchangers. *Journal of Materials Engineering and Performance*, *30*, 2876–2889.

Dahmani, M., Dahmani, A., Et-Touhami, S. S., Al-Deyab, B., Hammouti, A., & Bouyanzer. (2010). Microbial Synthesis of Zinc Oxide Nanoparticles. International Journal of Electrochemical Science, 17, 10–40.

Dang, Y. T., Power, A., Cozzolino, D., Dinh, K. B., Ha, B. S., Kolobaric, A., ... & Chapman, J. (2022). Analytical characterisation of material corrosion by biofilms. *Journal of Bio-and Tribo-Corrosion*, *8*(2), 50.

Donya, R., Mohd, Z. Bin, H.,& Yun, H. T. (2013). Synthesis and characterisation of ZnO nanostructures using palm olein as biotemplate. *Chemistry Central Journal*, *6*, 2–10.

Eddy, N O, Ameh, P.O., Gwarzo, I.J., Okop, I.J., & Dodo, S.N. (2013). Physicochemical Study and Corrosion Inhibition Potential of Ficus Tricopoda for Aluminium in Acidic Medium. *Portugaliae Electrochimica Acta* 31(2): 79–93. doi:10.4152/pea. 201302079.

Elemike E. E., Onwudiwe D. C. & Mbonu J. I. (2021). Facile synthesis of cellulose–ZnO-hybrid nanocomposite using Hibiscus rosa-sinensis leaf extract and its antibacterial activities. *Research journal of applied nanoscience*, *17*, 6.

Esquivel, J., & Gupta, R. K. (2020). corrosion-resistant metastable Al alloys: an overview of corrosion mechanisms. *Journal of The Electrochemical Society*, *167*(8), 081504.

Ezeibe, A. U., Nleonu, E. C., & Ahumonye, A. M. (2019). Thermodynamic study of the inhibitory action of lignin extract from Gmelina arborea on the corrosion of mild steel in dilute hydrochloric acid. *International Journal of Scientific Engineering and Research*, *7*(2), 133–136.

Fayomi, O. S. I., & Akande, I. G. (2018). Corrosion mitigation of aluminium in 3.65% NaCl medium using hexamine. *Journal of Bio-and Tribo-Corrosion*, *5*(1), 23.

Fayomi, O. S. I., Akande, I. G., & Sode, A. A. (2019). Corrosion prevention of metals via electroless nickel coating: A review. In *Journal of Physics: Conference Series* (Vol. 1378, No. 2, p. 022063). IOP Publishing.

Garg, B., Bisht, T., & Ling, Y. C. (2015). Graphene-based nanomaterials as efficient peroxidase Mimetic catalysts for biosensing applications: an overview. *Molecules*, *20*(8), 14155-14190.

Gayakwad, N., Patil, V., & Rao, B. M. (2022). The effect of Rhoeo discolour plant leaf extract on the corrosion inhibition of mild steel in acidic media. *Materials Today: Proceedings*, *49*, 536–541. https://doi.org/10.1016/j.matpr.2021.03.671

Gharpure, S., Yadwade, R., & Ankamwar, B. (2022). Non-antimicrobial and Non-anticancer Properties of ZnO Nanoparticles Biosynthesised Using Different Plant Parts of Bixa orellana. *ACS Omega*, *7*(2), 1914–1933. https://doi.org/10.1021/acsomega.1c05324

Goni, L. K., Yaagoob, I. Y., Mazumder, M. A., & Ali, S. A. (2024). Synergistic effect of KI on the corrosion inhibition of a poly (diallylammonium chloride)-based cyclocopolymer containing bis-cationic motifs for mild steel corrosion in 20% formic acid. *RSC advances*, *14*(14), 9725–9746.

Hairui, L., Peipei, K., Ying L., Y., Yanting H., X., J., X., C., Y., Q.F., T., R. & Xiao, W. (2020). Zinc oxide nanoparticles synthesised from Vernonia amygdalina show anti-inflammatory and antinociceptive activities in the mouse model. Artificial cell. *Journal of Nanomedicine and Biotechnology, 48*, 68–78.

Hamid, A., Fadhel, A., & Azara, S. (2022). Studying the effect of irradiation time on preparing zinc oxide nanoparticles prepared by the microwave method. *Digest Journal of Nanomaterials and Biostructures*, *17*(4), 1417–1422. https://doi.org/10.15251/DJNB.2022.174.1417

Hamidon, T. S., & Hussin, M. H. (2020). Susceptibility of hybrid sol-gel (TEOS-APTES) doped with caffeine as potent corrosion protective coatings for mild steel in 3.5 wt.% NaCl. *Progress in Organic Coatings*, *140*, 105478.

Hanaor, D. A. H., Ghadiri, M., Chrzanowski W.& Gan, Y. (2014). Scalable Surface Area Characterisation by Electrokinetic Analysis of Complex Anion Adsorption. *Journal of material science and biotechnology, 8*, 5-7.

HAque M. J., Bellah M. M., Hassan M. R., & Rahman S. (2020). Synthesis of ZnO nanoparticles by two different methods and comparison of their structural, antibacterial, photocatalytic and optical properties. *Journal of Nanotechnology, 23*, 12.

Hegazy, M.A., M. Abdallah, M.K. Awad, & M. Rezk. (2014). "Three Novel Di-Quaternary Ammonium Salts as Corrosion Inhibitors for API X65 Steel Pipeline in Acidic Solution. Part I: Experimental Results." *Corrosion Science* 81:5464. doi:10.1016/j.corsci.2013.12.010.

Hulla, J. E., Sahu, S. C., & Hayes, A. W. (2015). Nanotechnology: History and future. *Human & experimental toxicology*, *34*(12), 1318-1321.

Iravani, S. (2011). Green Synthesis of metal nanoparticles using plants. *International journal of applied chemistry, 13*, 38–50.

Ismail, M. A., Taha, K., M. A., & Khezami, L. (2018). ZnO Nanoparticles: Surface and X-ray Profile Analysis. *Journal of Ovonic Research, 15*, 381–393.

Ituen, E., Akaranta, O., & James, A. (2017). Evaluation of the performance of corrosion inhibitors using Adsorption Isotherm Models: An Overview. *Chem. Sci. Int. J*, *18*(1), 1-34.

JimohA.A., A. B.H.,Azeez S.O.,Ayipo Y.O,.Abdulsalam Z.A,Adebayo Z.F,Ajao A.T & Zakariyah. (2022). Biosynthesis of Ag and TiO2 nanoparticles and the evaluation of their antibacterial activities. *Inorganic Chemistry Communications V*, *141*, 2–3.

Junaedi S, K., Al-Amiery, A.A.H., Mohamad, A.B. & Takriff, M.S. (2012). Synthesis and Characterisation of Novel Corrosion Inhibitor Derived from Oleic Acid: 2-Amino 5Oleyl-1, 3, 4-Thiadiazol (AOT). *International journal of electrochemical science, 7,* 43–54.

Junaedi S, Al-amiery, A., Kadihum, A. & Mohamad, A. (2013). Inhibition Effects of a Synthesized Aminoantipyrine Derivative on the Corrosion of Mild Steel in Hydrochloric Acid Solution Together with Quantum Chemical Studies. *International journal of molecular science, 51*, 915–928.

Kalpana V. N., Kataru B. A. S., Sravani N, Vigneshwari T Panneerselvam A, & Rajeswari V. D. (2018). Biosynthesis of Zinc oxide nanoparticles using culture filtrates of Aspergillus niger: Antimicrobial textiles and dye degradation studies. *Journal of nanotechnology, 76*, 3.

Kamegawa, T., Ishiguro, Y., & Yamashita, H. (2019). Photocatalytic properties of TiO2-loaded porous silica with hierarchical macroporous and mesoporous architectures in the degradation of gaseous organic molecules. *Catalysis Today, 332*, 222–226.

Kumar, S., Manoj, P., & Giridhar, P. (2015). Fourier transform infrared spectroscopy (FTIR) analysis, chlorophyll content and antioxidant properties of native and defatted foliage of green leafy vegetables. *Journal of Food Science and Technology*, *52*, 8131–8139.

Kovo G. A., Soumya G., Marieka G. & Jeanet C. (2021). One-pot synthesis of zinc oxide nanoparticles via chemical precipitation for bromophenol blue adsorption and antifungal activity against filamentous fungi. *Scientific report, 15*, 8.

Liu, C. H., Lai, Y. X., Chen, J. H., Tao, G. H., Liu, L. M., Ma, P. P., & Wu, C. L. (2016). Natural-aging-induced reversal of the precipitation pathways in an Al–Mg–Si alloy. *Scripta Materialia*, *115*, 150-154.

Liu, P., Xu, Q., Zhang, Q., Huang, Y., Liu, Y., Li, H.,& Lei, G. (2024). A new insight into
Corrosion inhibition mechanism of the corrosion inhibitors: review on DFT and MD simulation. *Journal of Adhesion Science and Technology*, *38*(10), 1563-1584.

López C., & Rodríguez Páez, J. E. (2017). Synthesis and characterisation of ZnO nanoparticles: effect of solvent and antifungal capacity of NanoParticles obtained in ethylene glycol. *Journal of Applied Physics, 8*, 23–78.

Martin, R. W., Edwards, P. R., Donnell, K. P., Mackay, E. G., & Watson, I. M. (2002). Microcomposition and luminescence of InGaN emitters. *physica status solidi (a)*, *192*(1), 117-123.

Mohammed, Y., Faruruwa, M. D., Muhammad, A., & Haruna, A. S. (2024). Kinetics and Thermodynamics of Heavy Metal Adsorption using Activated Carbon Developed from Doum Palm Seeds. *Journal of Basics and Applied Sciences Research*, *2*(1), 177–194. https://doi.org/10.33003/jobasr-2024-v2i1-44

Morones J.R., Elechiguerra J.L.,& Camacho A . (2005). The bactericidal effect of silver nanoparticles. *Journal of Animal Science Biootechnology, 16*, –6-53.

Mureddu, M., Ferino, I., Musinu, A., Ardu, A., Rombi, E., Cutrufello, M. G., Deiana, P., Fantauzzi, M., & Cannas, C. (2014). MeO x /SBA-15 (Me = Zn, Fe): highly efficient nanosorbents for mid-temperature H 2 S removal. *J. Mater. Chem. A*, *2*(45), 19396–19406. https://doi.org/10.1039/C4TA03540B

Nzekekwu, A.K. & Abosede, O.O. (2019). Green Synthesis and Characterisation of Silver Nanoparticles Using Leaf Extracts of Neem (Azadirachta indica) and Bitter Leaf (Vernonia amygdalina). *Journal of Applied Science Environment Management, 23, 695–699.*

Oguzie, E., Li, Y., & Wang, F. (2007). Corrosion inhibition and adsorption behaviour of methionine on mild steel in sulfuric acid and the synergistic effect of iodide ion. Journal of Colloid Interface Science, 310, 90-98.

Pan, P., Chen, H., Liang, Z., & Zhao, Q. (2018). Deposition and corrosion characteristics of liquid-solid droplets on tubular corrosion probes in desulphurised flue gas. *Engineering Failure Analysis*, *90*, 129–140.

Pandey, A., Dalal, S., Dutta, S., & Dixit, A. (2021). Structural characterization of polycrystalline thin films by X-ray diffraction techniques. *Journal of Materials Science: Materials in Electronics*, *32*(2), 1341-1368.

Popov, B. N. (2015). Corrosion Inhibitors. In *Corrosion Engineering*, Elsevier, 581–97. doi:10.1016/B978-0-444-62722-3.00014-8.

Prami, N, & Debajyoti, D. (2019). Photocatalytic degradation of Rhodamine-B dye by stable ZnO nanostructures with different calcination temperatures, which induce defects. *Journal of Applied Surface Science, 43*, 465–556.

Quadri, T. W., Akpan, E. D., Olasunkanmi, L. O., Fayemi, O. E., & Ebenso, E. E. (2022). Fundamentals of corrosion chemistry. In *Environmentally sustainable corrosion inhibitors* (pp. 25-45). Elsevier.

Quan, B., Li, J., & Chen, C. (2021). Effect of Corrosion Temperature on the Corrosion of Q235 Steel and 16Mn Steel in Sodium Aluminate Solutions. *ACS Omega*, *6*(40), 25904–25915. https://doi.org/10.1021/acsomega.1c02220

Shukla, S. K., & Eno, E. E. (2011). Corrosion Inhibition, Adsorption Behaviour and Thermodynamic Properties of Streptomycin on Mild Steel in Hydrochloric Acid Medium. *International Journal of Electrochemical Science* 6(8): 3277–91. doi:10.1016/S1452-3981(23)18251-4.

Swenson, H., & Nicholas P. S. (2019). Langmuir's Theory of Adsorption: A Centennial Review *Langmuir* 35(16): 5409–26. doi:10.1021/acs.langmuir.9b00154.

Vaszilcsin, C. G., Putz, M. V., Kellenberger, A., & Dan, M. L. (2023). On the evaluation of metal-Corrosion inhibitor interactions by adsorption isotherms. *Journal of Molecular Structure*, *1286*, 135643.

YU, J. G., Wang, W. G.,& Cheng, B. (2010). Synthesis and enhanced photocatalytic activity of a Hierarchical porous flowerlike pn junction NiO/TiO2 photocatalyst. *Journal of Applied Chemistry, 5*, 23.

Zhao, Y.-L., Ye, F.-X., Zhang, G., Yao, J., Liu, Y.-F., & Dong, S.-G. (2022). Investigation of erosion-corrosion behaviour of Q235B steel in liquid-solid flows. *Petroleum Science*, *19*(5), 2358–2373. https://doi.org/10.1016/j.petsci.2022.05.020

Zehra, S., Mobin, M., & Aslam, J. (2022). An overview of the corrosion chemistry. *Environmentally Sustainable Corrosion Inhibitors*, 3-23.